Interfacial Area Transport of Vertical Upward Bubbly Two-Phase Flow in an Annulus

Takashi Hibiki [a, b, *], Ye Mi [b], Rong Situ [b], Mamoru Ishii [b]

[a] *Research Reactor Institute, Kyoto University, Kumatori, Sennan, Osaka 590-0494, Japan*

[b] *School of Nuclear Engineering, Purdue University, West Lafayette, IN 47907-1290, USA*

* Tel: +81-724-51-2373, Fax.: +81-724-51-2461, Email: hibiki@rri.kyoto-u.ac.jp

Abstract In relation to the development of the interfacial area transport equation in a subcooled boiling flow, the one-dimensional interfacial area transport equation was evaluated by the data taken in the hydrodynamic separate effect tests without phase change for an adiabatic air-water bubbly flow in a vertical annulus. The annulus channel consisted of an inner rod with a diameter of 19.1 mm and an outer round tube with an inner diameter of 38.1 mm, and the hydraulic equivalent diameter was 19.1 mm. Twenty data sets consisting of five void fractions, about 0.050, 0.10, 0.15, 0.20, and 0.25, and four superficial liquid velocities, 0.272, 0.516, 1.03, and 2.08 m/s were used for the evaluation of the one-dimensional interfacial area transport equation. The one-dimensional interfacial area transport equation agreed with the data with an average relative deviation of ±8.96 %. Sensitivity analysis was also performed to investigate the effect of the initial bubble size on the interfacial area transport. It was shown that the dominant mechanism of the interfacial area transport was strongly dependent of the initial bubble size.

Key Words: Interfacial area transport; Two-fluid model; Interfacial area concentration; Double-sensor conductivity probe; Gas-liquid bubbly flow; Multiphase flow

Nomenclature

A_i	interfacial area
a_i	interfacial area concentration
C	adjustable valuable
C_{RC}	adjustable valuable
C_{WE}	adjustable valuable
C_{TI}	adjustable valuable
D	diameter of outer round tube
D_0	diameter of inner rod
D_{bc}	critical bubble size
D_e	volume equivalent diameter
D_H	hydraulic equivalent diameter
D_{Sm}	Sauter mean diameter
$d\vec{x}$	spatial range
dV	volume range
f	particle density distribution function
j_g	superficial gas velocity
$j_{g,N}$	superficial gas velocity reduced at normal condition (atmospheric pressure and 20°C)
j_f	superficial liquid velocity
i_{fg}	latent heat
n	exponent
R	radius of outer round tube

R_0	radius of inner rod
R_j	rate of change of particle number density due to coalescence or breakup
r	radial coordinate
S_j	rate of change in the particle density distribution due to particle coalescence and breakup processes
S_{PH}	fluid particle source or sink rate due to phase change
T_f	liquid temperature
T_{sat}	saturation temperature
t	time
u_t	turbulent velocity
V	particle volume
V_{max}	maximum particle volume
V_{min}	minimum particle volume
$\overrightarrow{v_p}$	particle velocity
$\overrightarrow{v_g}$	gas velocity
v_g	gas velocity
v_{gz}	gas velocity in the z-direction
We	Weber number
We_{cr}	critical Weber number
$\vec{x}$	spatial position
z	axial coordinate

Greek symbols

α	void fraction
α	maximum void fraction
ρ_g	gas density
σ	interfacial tension
ϕ_{EXP}	rate of change of the interfacial area concentration due to bubble expansion
ϕ_j	rate of change of the interfacial area concentration due to bubble coalescence or breakup
ϕ_{PH}	rate of change of the interfacial area concentration due to phase change
ϕ_{RC}	rate of change of the interfacial area concentration due to bubble coalescence caused by bubble random collision
ϕ_{TI}	rate of change of the interfacial area concentration due to bubble breakup caused by turbulent impact
ϕ_W	rate of change of the interfacial area concentration due to wall nucleation
ϕ_{WE}	rate of change of the interfacial area concentration due to bubble coalescence caused by wake entrainment
ψ	factor depending on the shape of a bubble (1/(36π) for a spherical bubble)

Subscripts

calc.	calculated value
meas.	measured value
Probe	quantity measured by a double-sensor conductivity probe
Rotameter	quantity measured by a rotameter

γ-densitometer	quantity measured by a γ-densitometer

Mathematical symbols

$< >$	area-averaged quantity
$<< >>$	void fraction weighted cross-sectional area-averaged quantity
$<< >>_a$	interfacial are concentration weighted cross-sectional area-averaged quantity

1. Introduction

In relation to the modeling of the interfacial transfer terms in the two-fluid model, the concept of the interfacial area transport equation has recently been proposed to develop the constitutive relation on the interfacial area concentration [1]. The dynamic changes in the two-phase flow structure can be predicted mechanistically by introducing the interfacial area transport equation. Such a capability does not exist in the current state-of-the-art nuclear thermal-hydraulic system analysis codes like RELAP5, TRAC and CATHARE. Thus, a successful development of the interfacial area transport equation can make a quantum improvement in the two-fluid model formulation and the prediction accuracy of the system codes.

The present status of the development of the interfacial area transport equation was extensively reviewed in the previous paper [2]. In the first stage of the development of the interfacial area transport equation, adiabatic flow was the focus, and the interfacial area transport equation for the adiabatic flow was developed successfully by modeling sink and source terms of the interfacial area concentration due to bubble coalescence and breakup [3-5]. In the next stage, subcooled boiling flow would be the focus, and a preliminary local measurement for interfacial area concentration was initiated for subcooled boiling water flow in an internally heated annulus [6]. To develop the interfacial area transport equation for boiling flows in the internally heated annulus, sink and source terms due to phase change should be modeled based on rigorous and extensive boiling flow data to be taken in the annular channel, and sink and source terms due to bubble coalescence and breakup modeled previously [3] should be evaluated separately based on adiabatic data to be taken in the same channel.

From this point of view, this study aims at evaluating the one-dimensional interfacial area transport equation with axial development data of local flow parameters (void fraction,

interfacial area concentration, and interfacial velocity) of vertical upward air-water bubbly flows in an annulus. The annulus test loop is scaled to a prototypic BWR based on scaling criteria for geometric, hydrodynamic, and thermal similarities [6]. The data obtained from the double-sensor conductivity probe give near complete information on the time-averaged local hydrodynamic parameters of bubbly flow to evaluate the sink and source terms of the interfacial area concentration. The one-dimensional interfacial area transport equation is evaluated by the data set taken in the annulus loop. The detailed discussion is also given for the mechanism of the axial development of local flow parameters.

2. Interfacial area transport equation

For the purpose of modeling interfacial area transport, Kocamustafaogullari and Ishii [1] obtained the interfacial area transport equation based on statistical mechanics. The fluid particle number density distribution changes with the fluid particle contraction and expansion, entering and leaving, coalescence and disintegration, evaporation and condensation, nucleation and collapse. Simply accounting for these effects in a control volume yields the fluid particle transport equation:

$$\frac{\partial f}{\partial t} + \nabla \cdot \left(f \vec{v}_p \right) + \frac{\partial}{\partial V} \left(f \frac{dV}{dt} \right) = \sum_j S_j + S_{PH}, \qquad (1)$$

where $f\left(\vec{x}, V, t\right)$ is the particle density distribution function, which is assumed to be continuous and specifies the probable number density of fluid particles at a given time *t*, in the spatial range $d\vec{x}$ about a position $\vec{x}$, with particle volumes between *V* and *V*+*dV*. $\vec{v_p}\left(\vec{x}, V, t\right)$ denotes the particle velocity, a function of the position, $\vec{x}$, particle volume, *V*, and time, *t*. For small rigid bubbles, the particle velocity, $\vec{v}_p$, is identical to the gas velocity, $\vec{v}_g$. The interaction term,

$\sum_j S_j$, represents the net rate of change in the particle density distribution due to the particle coalescence and breakup processes. The second term of the right hand side, S_{PH}, is the fluid particle source or sink rate due to the phase change. For example, for a one-component bubbly flow, S_{PH} represents the bulk liquid bubble nucleation rate due to homogeneous and heterogeneous nucleation, and the collapse rate due to condensation for the subcooled boiling flow. The wall nucleation rate which is not included in S_{PH} must be specified as a boundary condition. The third term of the left-hand side in Eq.(1) represents the rate of change in the particle density distribution due to the pressure change and/or phase changes appearing on existing interfaces.

The interfacial area concentration transport equation of fluid particles can be obtained by multiplying the particle number density transport equation by the average interfacial area, $A_i(V)$, which is independent of the spatial coordinate system. This yields the following equation:

$$\frac{\partial f A_i(V)}{\partial t} + \nabla \cdot \left(f \vec{v}_g A_i(V) \right) + A_i(V) \frac{\partial}{\partial V} \left(f \frac{dV}{dt} \right) = \sum_j S_j A_i(V) + S_{PH} A_i(V). \quad (2)$$

For practical purposes, the fluid particle interfacial area transport equation is too detailed. Hence, it would be much more useful to average an interfacial area transport equation over particle size groups that are determined according to particle mobilities. As a general approach, two-group interfacial area transport equations have recently been proposed by treating the bubbles in two groups such as the spherical/distorted bubble group (group one) and the cap/slug bubble group (group two) [5]. If only one group of bubbles is considered, the interfacial area transport equation can easily be obtained by integrating Eq.(2) from V_{min} to V_{max} and applying the Leibnitz rule. Then, we have the three-dimensional interfacial transport equation:

$$\frac{\partial a_i}{\partial t}+\nabla\cdot\left(a_i\vec{v}_g\right)=\frac{2}{3}\frac{a_i}{\alpha}\left(\frac{\partial\alpha}{\partial t}+\nabla\cdot\alpha\vec{v}_g\right)+\frac{1}{3\psi}\left(\frac{\alpha}{a_i}\right)^2\sum_j R_j+\pi D_{bc}^2\left(1-\frac{2}{3}\left(\frac{D_{bc}}{D_{Sm}}\right)\right)R_{PH}\,, \tag{3}$$

where R_j is the rate of change of particle number due to coalescence or breakup, ψ is the shape factor defined by

$$\psi=\frac{1}{36\pi}\left(\frac{D_{Sm}}{D_e}\right)^3\,,\ \left(\psi=\frac{1}{36\pi}\ \text{for spherical bubbles}\right) \tag{4}$$

where D_e is the volume equivalent diameter, and D_{bc} is the critical bubble size beyond, which it is possible for bubbles to grow due to evaporation, or for clusters of molecules to serve as nuclei for bubbles, as.

$$D_{bc}=\frac{4\sigma T_{sat}}{\rho_g i_{fg}\left(T_f-T_{sat}\right)}. \tag{5}$$

where σ, T_{sat}, ρ_g, i_{fg}, and T_f are the surface tension, the saturation temperature, the gas density, the latent heat, and the liquid temperature, respectively. The simplest form of the one-group interfacial area transport equation is the one-dimensional formulation obtained by applying cross-sectional area averaging over Eq.(3). That is

$$\frac{\partial\langle a_i\rangle}{\partial t}+\frac{d}{dz}\left(\langle a_i\rangle\langle\langle v_{gz}\rangle\rangle_a\right)=\langle\phi_{EXP}\rangle+\sum_j\langle\phi_j\rangle+\langle\phi_{PH}\rangle+\langle\phi_W\rangle, \tag{6}$$

where $<\phi_{EXP}>$, $<\phi_j>$, and $<\phi_{PH}>$ are the rate of change of the interfacial area concentration due to bubble expansion, bubble coalescence or breakup, and phase change defined as Eqs.(7),(8),(9), respectively.

$$\langle\phi_{EXP}\rangle\equiv\left(\frac{2\langle a_i\rangle}{3\langle\alpha\rangle}\right)\left\{\frac{\partial\langle\alpha\rangle}{\partial t}+\frac{d\langle\alpha\rangle\langle\langle v_{gz}\rangle\rangle}{dz}\right\}, \tag{7}$$

$$\left\langle \phi_j \right\rangle \equiv \frac{1}{3\psi}\left(\frac{\left\langle \alpha \right\rangle}{\left\langle a_i \right\rangle}\right)^2 \left\langle R_j \right\rangle, \tag{8}$$

$$\left\langle \phi_{PH} \right\rangle \equiv \pi D_{bc}^2 \left\{1-\frac{2}{3}\left(\frac{D_{bc}}{\left\langle D_{Sm} \right\rangle}\right)\right\}. \tag{9}$$

$<\phi_W>$ is the wall nucleation source, which is the most important term for subcooled boiling flow. For gas-dispersed flows with no phase change, three major mechanisms are responsible for bubble coalescence and breakup that result in the interfacial area transport [3]. They are (1) bubble coalescence due to random collision driven by liquid turbulence, $<\phi_{RC}>$, (2) bubble coalescence due to wake-entrainment caused by the relative motion between the bubbles in the wake region and the leading bubble, $<\phi_{WE}>$ and (3) bubble breakup upon the impact of turbulent eddies, $<\phi_{TI}>$. The source and sink terms of the interfacial area in Eq.(6) can be expressed as follows [3]:

$$\left\langle \phi_{RC} \right\rangle = 12\psi C_{RC}\left[\frac{\left\langle u_t \right\rangle \left\langle a_i \right\rangle^2}{\left\langle \alpha \right\rangle_{\max}^{1/3}\left(\left\langle \alpha \right\rangle_{\max}^{1/3}-\left\langle \alpha \right\rangle^{1/3}\right)}\right]\left[1-\exp\left(-\frac{C\left\langle \alpha \right\rangle_{\max}^{1/3}\left\langle \alpha \right\rangle^{1/3}}{\left\langle \alpha \right\rangle_{\max}^{1/3}-\left\langle \alpha \right\rangle^{1/3}}\right)\right], \tag{10}$$

$$\left\langle \phi_{WE} \right\rangle = 12\psi C_{WE}\left(\left\langle u_r \right\rangle \left\langle a_i \right\rangle^2\right), \tag{11}$$

$$\left\langle \phi_{TI} \right\rangle = \frac{1}{18}C_{TI}\left[\frac{\left\langle u_t \right\rangle \left\langle a_i \right\rangle^2}{\left\langle \alpha \right\rangle}\right]\left[1-\frac{We_{cr}}{We}\right]^{1/2}\exp\left(-\frac{We_{cr}}{We}\right), \quad We > We_{cr}. \tag{12}$$

where C_{RC}(=0.0041), C(=3.0), C_{WE}(=0.0020), C_{TI}(=0.035) are adjustable valuables determined based on extensive data set taken in various adiabatic bubbly flows. u_t, α_{max}, u_r, We, and We_{cr} are the turbulent velocity, the maximum allowable void fraction (=0.80), the relative velocity between gas and liquid, Weber number and critical Weber number, respectively.

3. Experimental

An experimental facility is designed to measure the relevant two-phase parameters necessary for developing constitutive models for the two-fluid model in subcooled boiling. It is scaled to a prototypic BWR based on scaling criteria for geometric, hydrodynamic, and thermal similarities [6]. The experimental facility, instrumentation, and data acquisition system are briefly described in this section. The detailed explanation can be found in the previous paper [6].

The two-phase flow experiment was performed by using a flow loop constructed at Thermal-Hydraulics and Reactor Safety Laboratory in Purdue University. Figure 1 shows the experimental facility layout. The water supply is held in the main tank. The tank is open to the atmosphere through a heat exchanger mounted to the top to prevent explosion or collapse and to degas from the water. There is a cartridge heater inside the tank to heat the water and maintain the inlet water temperature. A cooling line runs inside the tank to provide control of the inlet water temperature and post-experimental cooling of the tank. Water is pumped with a positive displacement, eccentric screw pump, capable of providing a constant head with minimum pressure oscillation. The water, which flows through a magnetic flow meter, is divided into four separate flows and can then be mixed with air before it is injected into the test section to study adiabatic air-water bubbly flow. For the adiabatic air-water flow experiment, porous spargers with the pore size of 10 μm are used as air injectors. The test section is an annular geometry that is formed by a clear polycarbonate tube on the outside and a cartridge heater on the inside. The test section is 38.1 mm inner diameter, D, and has a 3.18 mm wall thickness. The overall length of the heater is 2670 mm and has a 19.1 mm outer diameter, D_0. The heated section of the heater rod is 1730 mm long. The maximum power of the heater is 20 kW and has a

maximum surface heat flux of 0.193 MW/m^2. The heater rod has one thermocouple that is connected to the process controller to provide feedback control. The heater rod can be traversed vertically to allow many axial locations to be studied with four instrument ports attached to the test section. At each port there is an electrical conductivity probe to measure axial development of local flow parameters. A pressure tap and thermocouple are placed at the inlet and exit of the test section. A differential pressure cell is connected between the inlet and outlet pressure taps. The loop can also be operated with a diabatic steam-water flow in a future study. The two-phase mixture flows out of the test section to a separator tank and the gas phase is piped away and the water is returned to the main tank.

The flow rates of the air and water were measured with a rotameter and a magnetic flow meter, respectively. The loop temperature was kept at a constant temperature (20 °C) within the deviation of ± 0.2 °C by a heat exchanger installed in a water reservoir. The local flow measurements using the double-sensor conductivity probe [7] were performed at four axial locations of z/D_H=40.3, 61.7, 77.7, and 99.0, and ten radial locations from $r/(R-R_0)$=0.05 to 0.9. A γ–densitometer was installed at z/D_H=51.1 in the loop to measure the area-averaged void fraction. The flow conditions in this experiment are tabulated in Table 1. The area-averaged superficial gas velocities in this experiment were roughly determined so as to provide the same area-averaged void fractions among different conditions of superficial liquid velocity, namely $<\alpha>$=0.050, 0.10, 0.15, 0.20, and 0.25. It should be noted here that void fraction would increase along the axial direction on the order of 10 % between z/D_H=40.3 and 99.0 in the present experimental conditions due to the pressure reduction. This leads to a continuous developing flow along the flow direction.

Generally, a void distribution depends on an initial condition (bubble size, generation

method and mixing condition), a flow condition (flow rates and physical properties), and a test section condition (geometry and wall surface) [8]. Among them, the conditions except for the initial condition are the same in this experiment. Although sophisticated experiments controlling the initial condition were performed [8], the initial condition was not controlled in this experiment, resulting in the change of the initial bubble size with the flow condition. Figure 2 shows the dependence of the Sauter mean diameter, $<D_{Sm}>$, measured at the first measuring station of z/D_H=40.3 on the void fraction, $<\alpha>$, or the superficial liquid velocity, $<j_f>$. The bubble size measured at the first measuring station increased with increasing the gas flow rate, but the effect of the gas flow rate on the bubble size came to be smaller for higher liquid flow rate. On the other hand, the bubble size increased with increasing the liquid flow rate for $<j_f><0.5$ m/s and $<\alpha>\leq 0.10$, but the bubble size decreased with increasing the liquid flow rate for $<j_f>\geq 1.0$ m/s. The increase in the gas flow rate or the increase in the liquid flow rate for $<j_f><0.5$ m/s and $<\alpha>\leq 0.15$ would enhance the bubble coalescence due to the collision of bubbles, resulting in the increase of the bubble size. On the other hand, the increase in the liquid flow rate for $<j_f>\geq 1$ m/s would enhance the bubble breakup due to the liquid turbulence, resulting in the decrease of the bubble size. However, the effect of the liquid flow rate on the bubble size was not pronounced for $<j_f>\leq 1$ m/s, where the liquid turbulence might not be large enough to disintegrate the bubbles. In this experiment, bubbles with the diameters of about 3 mm and 2 mm were generated for $<j_f>\leq 1$ m/s and $<j_f>=2$ m/s, respectively. The similar result was obtained for vertical air-water bubbly flow in a round tube with an inner diameter of 50.8 mm [9].

In order to verify the accuracy of local measurements, the area-averaged quantities obtained by integrating the local flow parameters over the flow channel were compared with those measured by other cross-calibration methods such as a γ-densitometer for void fraction, a

photographic method for interfacial area concentration, and a rotameter for superficial gas velocity. As shown in Fig.3, good agreements were obtained between the area-averaged void fraction and superficial gas velocity obtained from the local measurements and those measured by the cross-calibration methods with averaged relative deviations of ±12.8 % and ±14.9 %, respectively. The separate experiment to evaluate the interfacial area concentration measured by the double sensor probe with the photographic method showed a good agreement between the area-averaged interfacial area concentration obtained from the double sensor probe method and that measured by the photographic method with an averaged relative deviation of ±6.95 % [10].

4. Results and discussion

4.1. Axial Development of Local Flow Parameters

Some discussions on the flow characteristics of local flow parameters for gas and liquid phases in an annulus can be found in the previous papers [11, 12]. Here, the axial development of the local flow parameters will briefly be described as follows.

4.1.1. Void Fraction

Figure 4 shows the behavior of void fraction profiles measured at z/D_H=40.3 (upper figures) and 99.0 (lower figures) in this experiment. The meanings of the symbols in Fig.4 are found in Table 1. As can be seen from the figure, various phase distribution patterns similar to those in round tubes are observed in the present experiment, and void fraction profiles are found to be almost symmetrical with respect to the channel center, $r/(R\text{-}R_0)$=0.5. For $\langle j_f \rangle$=0.272 m/s, broad core peak with plateau around the channel center and intermediate peak, which is characterized as broad peak in void fraction near the channel wall and plateau with medium void fraction around the channel center, are found for low (●,▲) and high (■,▼,◆) void fraction

regions, respectively, at the first measuring station of z/D_H=40.3. As the flow develops, the plateau observed for low void fraction region (●,▲) tends to be narrower. On the other hand, as the flow develops, two peaks observed for high void fraction region (■,▼,◆) tend to move towards the channel center and to be merged into one core peak. For $<j_f>$=0.516 m/s, intermediate peak is observed at the first measuring station of z/D_H=40.3. As the flow develops, the void fraction profiles are not changed for low void fraction region (●,▲), but the trough of the void fraction profiles observed around the channel center comes to be shallower for high void fraction region (■,▼,◆). The similar tendency is observed for $<j_f>$=1.03 m/s. For $<j_f>$=2.08 m/s, wall peak is observed at the first measuring station of z/D_H=40.3. As the flow develops, the void fraction profiles are not changed. For $<j_f>$=0.272, 0.516, and 1.03 m/s, the bubble diameter is about 3 mm, which is close to a critical bubble size of 3.6 mm pointed out by Zun [13], which gives the boundary between the wall and intermediate peaks. The bubble size is likely to determine the direction of the bubble migration. Thus, in these cases, bubbles tend to move towards the channel center gradually. For $<j_f>$=2.08 m/s, the bubble diameter is about 2 mm, and can be stayed near the channel wall, resulting in insignificant axial change of the void fraction distribution.

4.1.2. Sauter mean diameter

Figure 5 shows the behavior of Sauter mean diameter profiles, corresponding to that of void fraction profiles in Fig.2. The meanings of the symbols in Fig.5 are found in Table 1. The Sauter mean diameter profiles are uniform along the channel radius with some decrease in size near the wall, $r/(R-R_0)\leq 0.1$ and $0.9\leq r/(R-R_0)$. Only a part of a bubble can pass the region close to the channel wall, resulting in apparent smaller Sauter mean diameter. The profiles are not changed significantly as the flow develops, although the bubble size increases up to 10-20 %

along the flow direction.

4.1.3. Interfacial area concentration

Figure 6 shows the behavior of interfacial area concentration profiles, corresponding to that of void fraction profiles in Fig.4. The meanings of the symbols in Fig.6 are found in Table 1. As can be expected for bubbly flow, the interfacial area concentration profiles are similar to the void fraction profiles. The interfacial area concentration is directly proportional to the void fraction and inversely proportional to the Sauter mean diameter. Thus, since the Sauter mean diameter is almost uniform along the channel radius, the interfacial area concentration profiles displayes the same behavior as their respective void fraction profiles.

4.1.5. Interfacial velocity

Figure 7 shows the behavior of interfacial velocity profiles, corresponding to that of void fraction profiles in Fig.4. The meanings of the symbols in Fig.7 are found in Table 1. As can be expected, the interfacial velocity has a power-law profile. As shown in the figure, measured interfacial velocities can be fitted by the following function reasonably well except for $\langle j_f \rangle$=2.08 m/s and higher void fraction.

$$v_g = \frac{n+1}{n}\langle v_g \rangle \left\{ 1 - \left| \frac{2r - (R - R_0)}{R - R_0} \right| \right\}^{1/n} . \qquad (13)$$

As the area-averaged void fraction increases, the exponent increases gradually, resulting in flatter interfacial velocity profile. As the superficial liquid velocity increases, the exponent decreases gradually and approaches an asymptotic value. Since the interfacial velocity would have the same tendency of the respective liquid velocity profile [9], the interfacial velocity profile might be attributed to the balance of the bubble-induced turbulence and shear-induced turbulence. It was observed in a round tube that for low liquid superficial velocities ($\langle j_f \rangle \leq$1 m/s) the

introduction of bubbles into the liquid flow flattened the liquid velocity profile and the liquid velocity profile approached to that of developed single-phase flow with the increase of void fraction [9]. It was also reported that the effect of the bubble introduction into the liquid on the liquid velocity profile was diminishing with increasing gas and liquid velocities and for high liquid velocities ($<j_f>\geq 1$ m/s) the liquid velocity profile came to be the power law profile as the flow developed. Thus, for low or high liquid velocity, the bubble-induced or shear-induced turbulence would play an important role in determining the liquid velocity profile, respectively.

4.2. One-dimensional Interfacial Area Transport

4.2.1. Model Evaluation

Figure 8 shows the comparison of the one-dimensional one-group interfacial area transport equation with the 20 data sets measured in the annulus loop. It can be recognized that the one-dimensional one-group interfacial area transport equation can reproduce proper trends of the interfacial area transport depending on flow parameters. As shown in Fig.9, the one-dimensional one-group interfacial area transport equation gives excellent predictions of the interfacial area concentrations ranging over one order with an average relative deviation of ±8.96 %.

In order to evaluate the contribution of each source or sink term to interfacial area transport, the interfacial area concentration change due to each mechanism along the axial direction is calculated. Figure 10, 11 and 12 shows the contributions of bubble random collision, wake entrainment and bubble expansion to the interfacial area transport, respectively. Since the values of Weber number in the present experiment are smaller than the critical Weber number, the values of $<\phi_{TI}>$ are calculated to be zero. As a general trend, the bubble expansion term, $<\phi_{EXP}>$,

governs the interfacial area transport at relatively low liquid velocity and void fraction, where bubble-bubble and bubble-eddy interactions are weak. The bubble coalescence terms, $<\phi_{RC}>$ and $<\phi_{WE}>$, are enhanced in the interfacial area transport equation at high void fraction, where the distance between bubbles is short enough to cause the bubble coalescence. It can be seen from these figures, the interfacial area concentration decrease rates due to the bubble coalescence terms, $<\phi_{RC}>$ and $<\phi_{WE}>$ are almost comparable to the interfacial area concentration increase rates due to the bubble expansion term, $<\phi_{EXP}>$ for most of the present experimental conditions. These consequently lead to insignificant interfacial area transport along the flow direction for most of the present experimental conditions as shown in Fig.8.

4.2.2. Sensitivity Analysis on Initial Bubble Size

The sensitivity analysis of the initial bubble size to the interfacial area concentration is performed to investigate the effect of the initial bubble size on the interfacial area transport. Figure 13 depicts an example of the sensitivity analysis for $<j_{g,N}>$=0.910 m/s and $<j_f>$=2.08 m/s. As can be seen from Figs.10-12, experimentally observed dominant mechanism on the interfacial area transport is bubble coalescence for $\left\langle D_{Sm,meas.}\right\rangle_{z/D_H=40.3}$=2.10 mm. When smaller bubbles such as $\left\langle D_{Sm,meas.}\right\rangle_{z/D_H=40.3}$=1.0 mm are generated at the inlet, the bubble coalescence is enhanced significantly, see the broken line. On the other hand, when larger bubbles such as $\left\langle D_{Sm,meas.}\right\rangle_{z/D_H=40.3}$=3.0 mm are generated at the inlet, the dominant mechanism on the interfacial area transport becomes bubble breakup instead of bubble coalescence, see the chain line. Thus, the dominant mechanism of the interfacial area transport is strongly dependent of the initial bubble size, and the interfacial area transport equation can reproduce the dependence of the initial bubble size on the interfacial area transport reasonably.

6. Conclusions

As a first step of the development of the interfacial area transport equation in a subcooled boiling flow, the one-dimensional interfacial area transport equation was evaluated by the data taken in the hydrodynamic separate tests without phase change for an adiabatic air-water bubbly flow in a vertical annulus. The annulus channel consisted of an inner rod with a diameter of 19.1 mm and an outer round tube with an inner diameter of 38.1 mm, and the hydraulic equivalent diameter was 19.1 mm. Twenty data sets consisting of five void fractions, about 0.050, 0.10, 0.15, 0.20, and 0.25, and four superficial liquid velocities, 0.272, 0.516, 1.03, and 2.08 m/s were used for the evaluation of the one-dimensional interfacial area transport equation. The one-dimensional interfacial area transport equation agreed with the data with an average relative deviation of ±8.96 %. Sensitivity analysis was also performed to investigate the effect of the initial bubble size on the interfacial area transport. It was shown that the dominant mechanism of the interfacial area transport was strongly dependent of the initial bubble size.

Acknowledgments

The research project was supported by the Tokyo Electric Power Company (TEPCO). The authors would like to express their sincere appreciation for the support and guidance from Dr. Mori of the TEPCO.

References

[1] G. Kocamustafaogullari, M. Ishii, Foundation of the interfacial area transport equation

and its closure relations, International Journal of Heat and Mass Transfer 38 (1995) 481-493.

[2] T. Hibiki, M. Ishii, Development of one-group interfacial area transport equation in bubbly flow systems, International Journal of Heat and Mass Transfer 45 (2002) 2351-2372.

[3] Q. Wu, S. Kim, M. Ishii, S. G. Beus, One-group interfacial area transport in vertical bubbly flow, International Journal of Heat and Mass Transfer 41 (1998) 1103-1112.

[4] T. Hibiki, M. Ishii, One-group interfacial area transport of bubbly flows in vertical round tubes, International Journal of Heat and Mass Transfer 43 (2000) 2711-2726.

[5] T. Hibiki, M. Ishii, Two-group interfacial area transport equations at bubbly-to-slug flow transition in a vertical round pipe, Nuclear Engineering and Design 202 (2000) 39-76.

[6] M. D. Bartel, M. Ishii, T. Masukawa, Y. Mi, R. Situ, Interfacial area measurements in subcooled flow boiling, Nuclear Engineering and Design 210 (2001) 135-155.

[7] S. Kim, X. Y. Fu, X. Wang, M. Ishii, Development of the miniaturized four-sensor conductivity probe and the signal processing scheme, International Journal of Heat and Mass Transfer 43 (2000) 4101-4118.

[8] A. Serizawa, I. Kataoka, Phase distribution in two-phase flow, Transient Phenomena in Multiphase Flow, Hemisphere, Washington, DC, 1988, pp.179-224.

[9] T. Hibiki, M. Ishii, Z. Xiao, Axial interfacial area transport of vertical bubbly flows, International Journal of Heat and Mass Transfer 44 (2001) 1869-1888.

[10] T. Hibiki, S. Hogsett, M. Ishii, Local measurement of interfacial area, interfacial velocity and liquid turbulence in two-phase flow, Nuclear Engineering and Design 184 (1998) 287-304.

[11] T. Hibiki, R. Situ, Y. Mi, M. Ishii, Experimental study on interfacial area transport in vertical upward bubbly two-phase flow in an annulus, International Journal of Heat and Mass Transfer (in print).

[12] R. Situ, T. Hibiki, Y. Mi, M. Ishii, M. Mori, Structure of air-water bubbly flow in a vertical annulus, Proceedings of the International Congress on Advanced Power Plants, Hollywood, Florida (2002).

[13] I. Zun, Transition from wall void peaking to core void peaking in turbulent bubbly flow, in : N. H. Afgan (Ed.), Transient Phenomena in Multiphase Flow, Hemisphere, Washington, DC, 1988, pp.225-245.

Caption of Table

Table 1. Flow conditions in this experiment.

Captions of Figures

Fig.1 Schematic diagram of experimental loop.

Fig.2 Dependence of bubble size on void fraction and superficial liquid velocity.

Fig.3. Verification of the double sensor probe with other calibration methods.

Fig.4. Local void fraction profiles at z/D_H=40.3 and 99.9.

Fig.5. Local Sauter mean diameter profiles at z/D_H=40.3 and 99.9.

Fig.6. Local interfacial area concentration profiles at z/D_H=40.3 and 99.9.

Fig.7. Local interfacial velocity profiles at z/D_H=40.3 and 99.9.

Fig.8. Evaluation of one-dimensional interfacial area transport equation with data.

Fig.9. Comparison of predicted and measured interfacial area concentrations.

Fig.10. Contribution of bubble coalescence due to bubble random collision to interfacial area transport.

Fig.11. Contribution of bubble coalescence due to wake entrainment to interfacial area transport.

Fig.12. Contribution of bubble expansion to interfacial area transport.

Fig.13 Sensitivity analysis on initial bubble to interfacial area transport.

Table 1 Flow conditions in this experiment.

Symbols	●	▲	■	▼	◆
$\langle j_f \rangle$ [m/s]	$\langle j_{g,N} \rangle$ [m/s]	$\langle j_{g,N} \rangle$ [m/s]	$\langle j_{g,N} \rangle$ [m/s]	$\langle j_{g,N} \rangle$ [m/s]	$\langle j_{g,N} \rangle$ [m/s]
0.272	0.0313	0.0506	0.0690	0.0888	0.105
0.516	0.0406	0.0687	0.103	0.135	0.176
1.03	0.0683	0.130	0.201	0.400	0.489
2.08	0.108	0.215	0.505	0.651	0.910

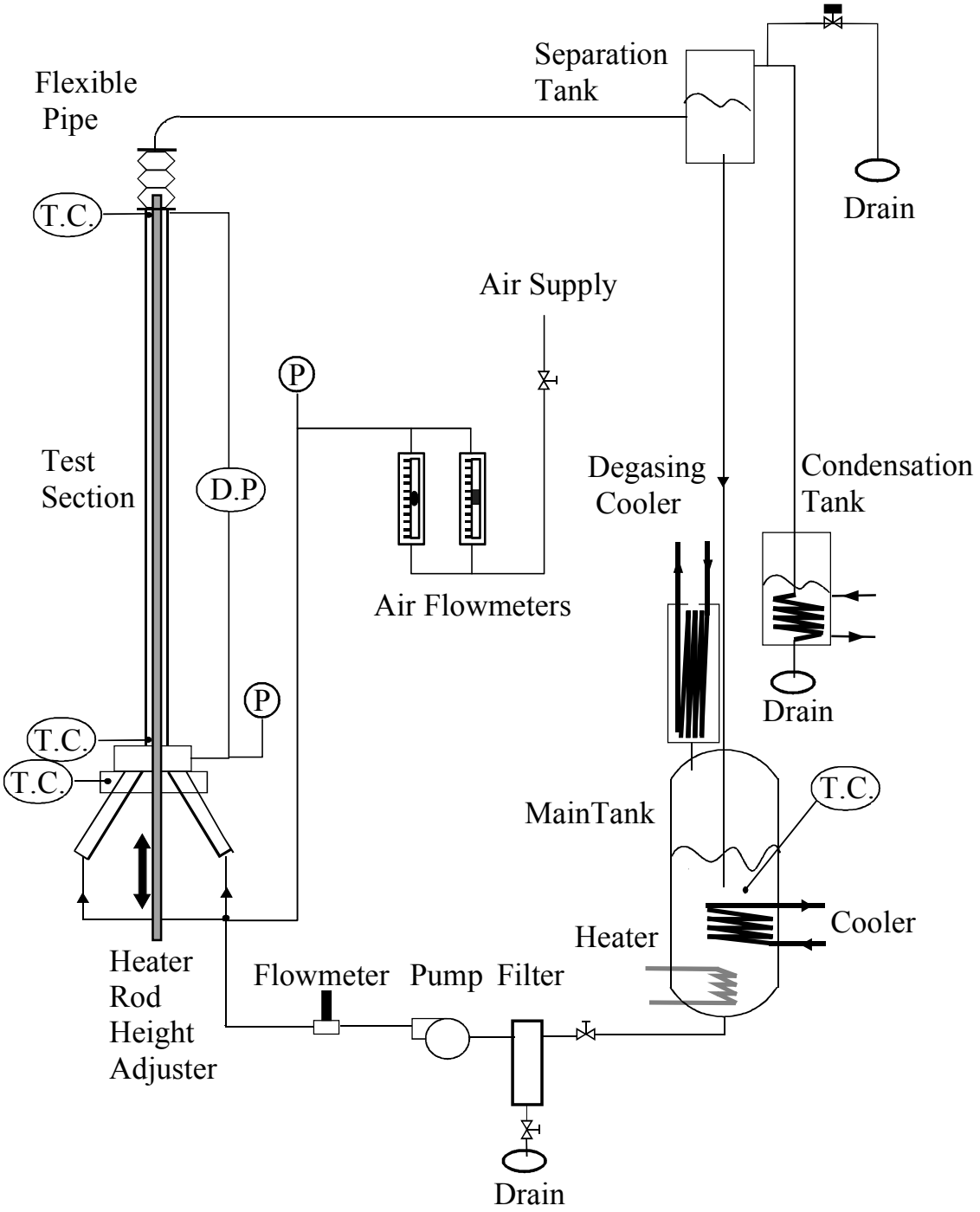
Separation
Tank
Flexible
Pipe
Drain
T.C.
Air Supply
P
Test
Section
D.P
Degasing
Cooler
Condensation
Tank
Air Flowmeters
Drain
P
T.C.
T.C.
MainTank
T.C.
Heater
Cooler
Heater
Rod
Height
Adjuster
Flowmeter
Pump
Filter
Drain

Fig.1

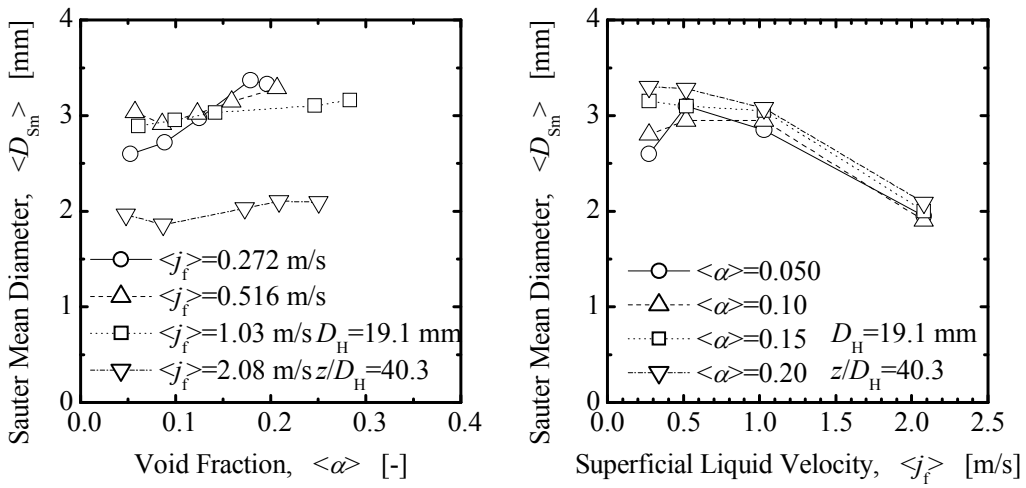
Sauter Mean Diameter, <D_{Sm}> [mm]
Void Fraction, <α> [-]
<j_f>=0.272 m/s
<j_f>=0.516 m/s
<j_f>=1.03 m/s
<j_f>=2.08 m/s
D_H=19.1 mm
z/D_H=40.3
Superficial Liquid Velocity, <j_f> [m/s]
<α>=0.050
<α>=0.10
<α>=0.15
<α>=0.20

Fig.2

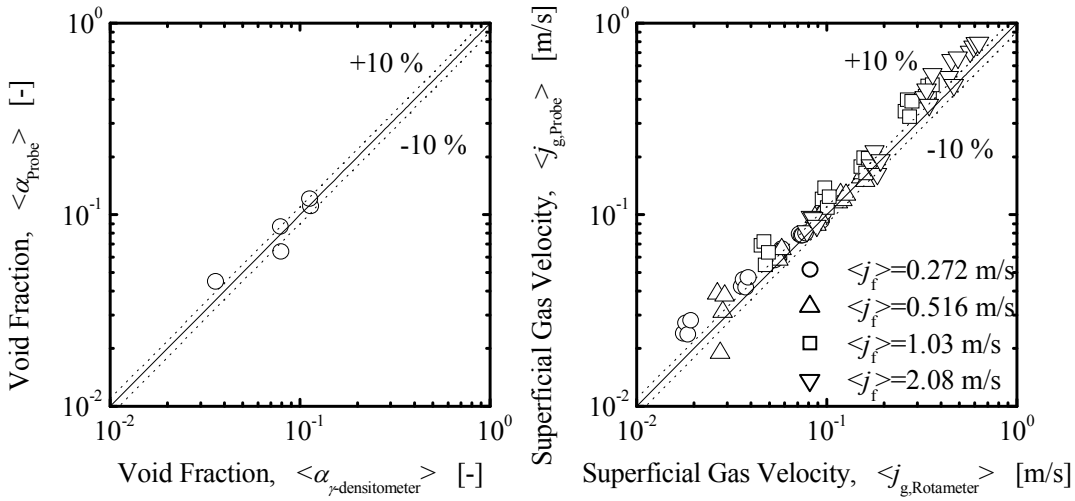
Void Fraction, <α_{Probe}> [-]
+10 %
-10 %
Void Fraction, <$\alpha_{\gamma\text{-densitometer}}$> [-]
Superficial Gas Velocity, <$j_{g,Probe}$> [m/s]
+10 %
-10 %
<j_f>=0.272 m/s
<j_f>=0.516 m/s
<j_f>=1.03 m/s
<j_f>=2.08 m/s
Superficial Gas Velocity, <$j_{g,Rotameter}$> [m/s]

Fig.3

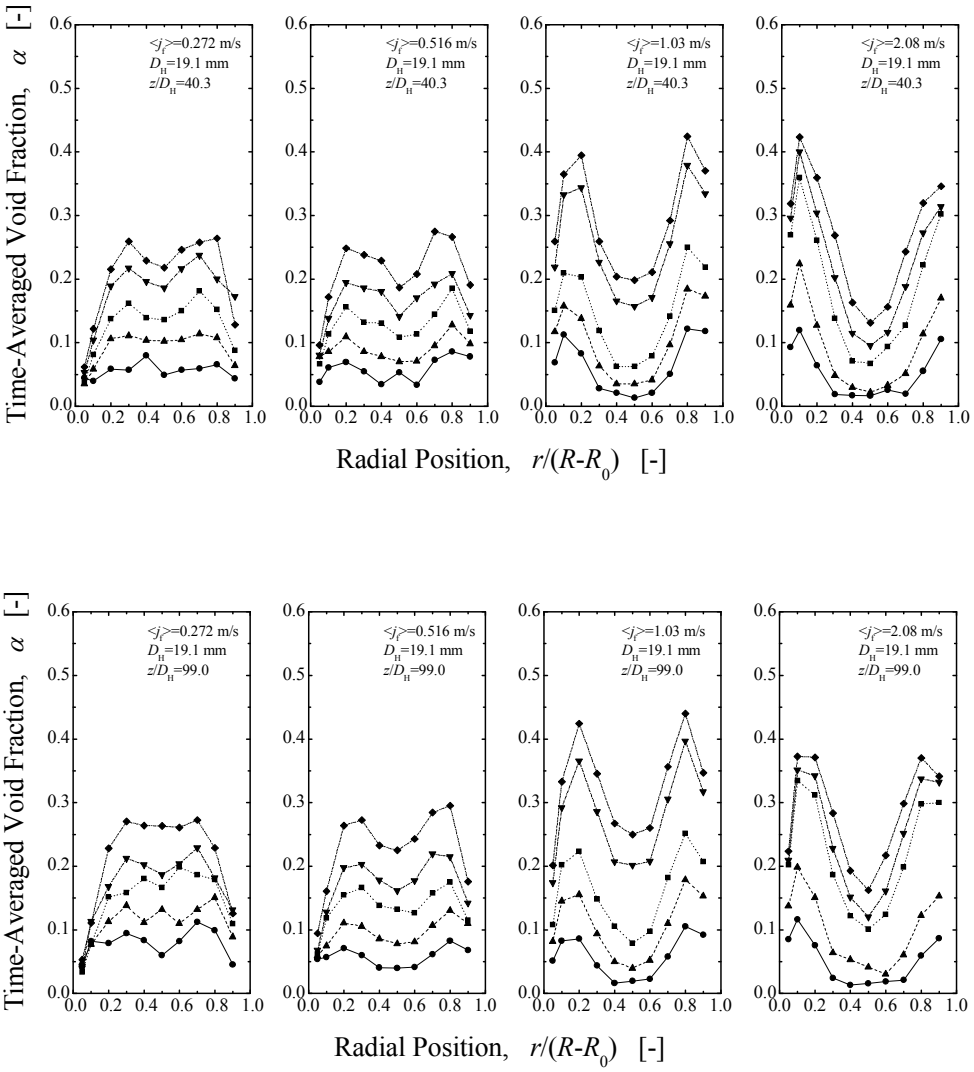
Time-Averaged Void Fraction, α [-]
<jf>=0.272 m/s
DH=19.1 mm
z/DH=40.3
<jf>=0.516 m/s
DH=19.1 mm
z/DH=40.3
<jf>=1.03 m/s
DH=19.1 mm
z/DH=40.3
<jf>=2.08 m/s
DH=19.1 mm
z/DH=40.3
Radial Position, r/(R-R0) [-]
Time-Averaged Void Fraction, α [-]
<jf>=0.272 m/s
DH=19.1 mm
z/DH=99.0
<jf>=0.516 m/s
DH=19.1 mm
z/DH=99.0
<jf>=1.03 m/s
DH=19.1 mm
z/DH=99.0
<jf>=2.08 m/s
DH=19.1 mm
z/DH=99.0
Radial Position, r/(R-R0) [-]

Fig.4

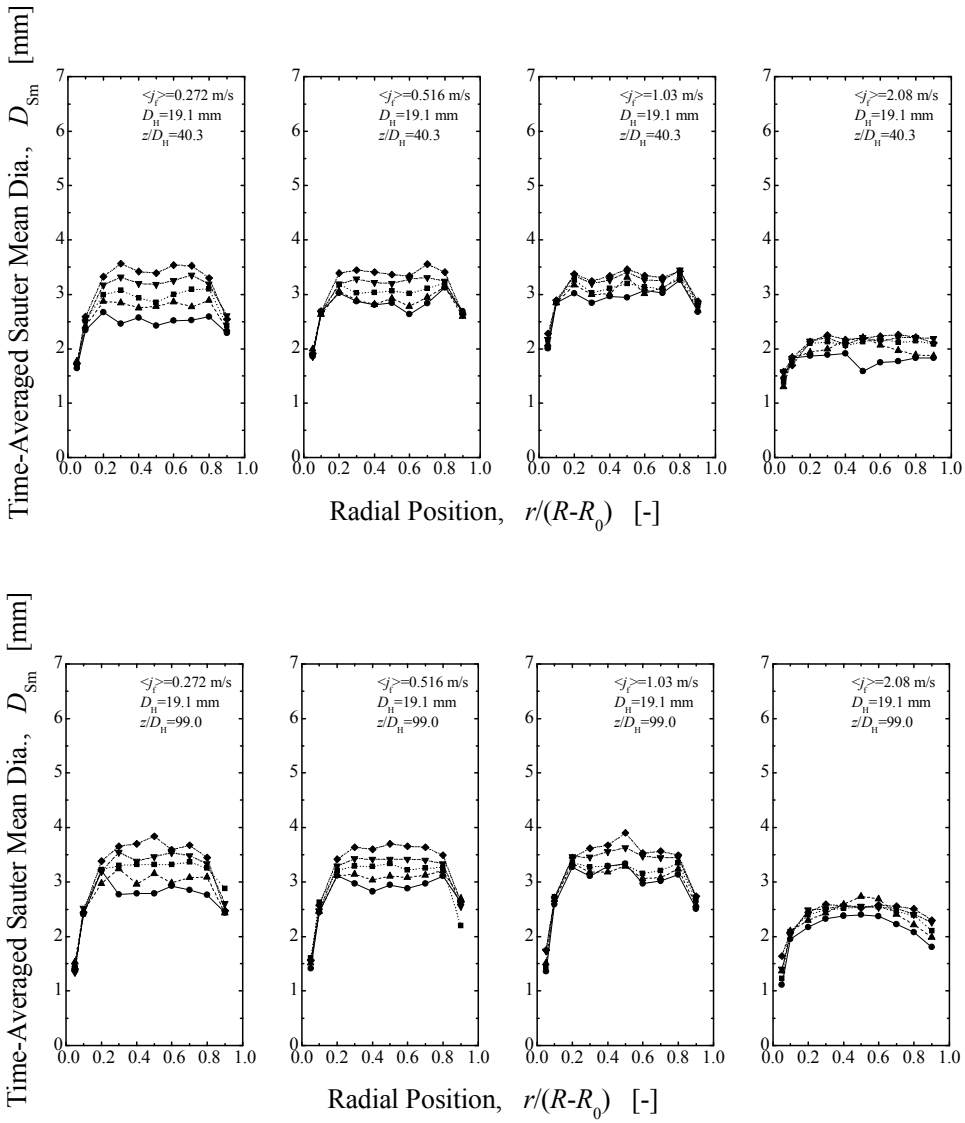
Time-Averaged Sauter Mean Dia., D_{Sm} [mm]
$<j_f>$=0.272 m/s
D_H=19.1 mm
z/D_H=40.3
$<j_f>$=0.516 m/s
D_H=19.1 mm
z/D_H=40.3
$<j_f>$=1.03 m/s
D_H=19.1 mm
z/D_H=40.3
$<j_f>$=2.08 m/s
D_H=19.1 mm
z/D_H=40.3
Radial Position, $r/(R-R_0)$ [-]
Time-Averaged Sauter Mean Dia., D_{Sm} [mm]
$<j_f>$=0.272 m/s
D_H=19.1 mm
z/D_H=99.0
$<j_f>$=0.516 m/s
D_H=19.1 mm
z/D_H=99.0
$<j_f>$=1.03 m/s
D_H=19.1 mm
z/D_H=99.0
$<j_f>$=2.08 m/s
D_H=19.1 mm
z/D_H=99.0
Radial Position, $r/(R-R_0)$ [-]

Fig.5

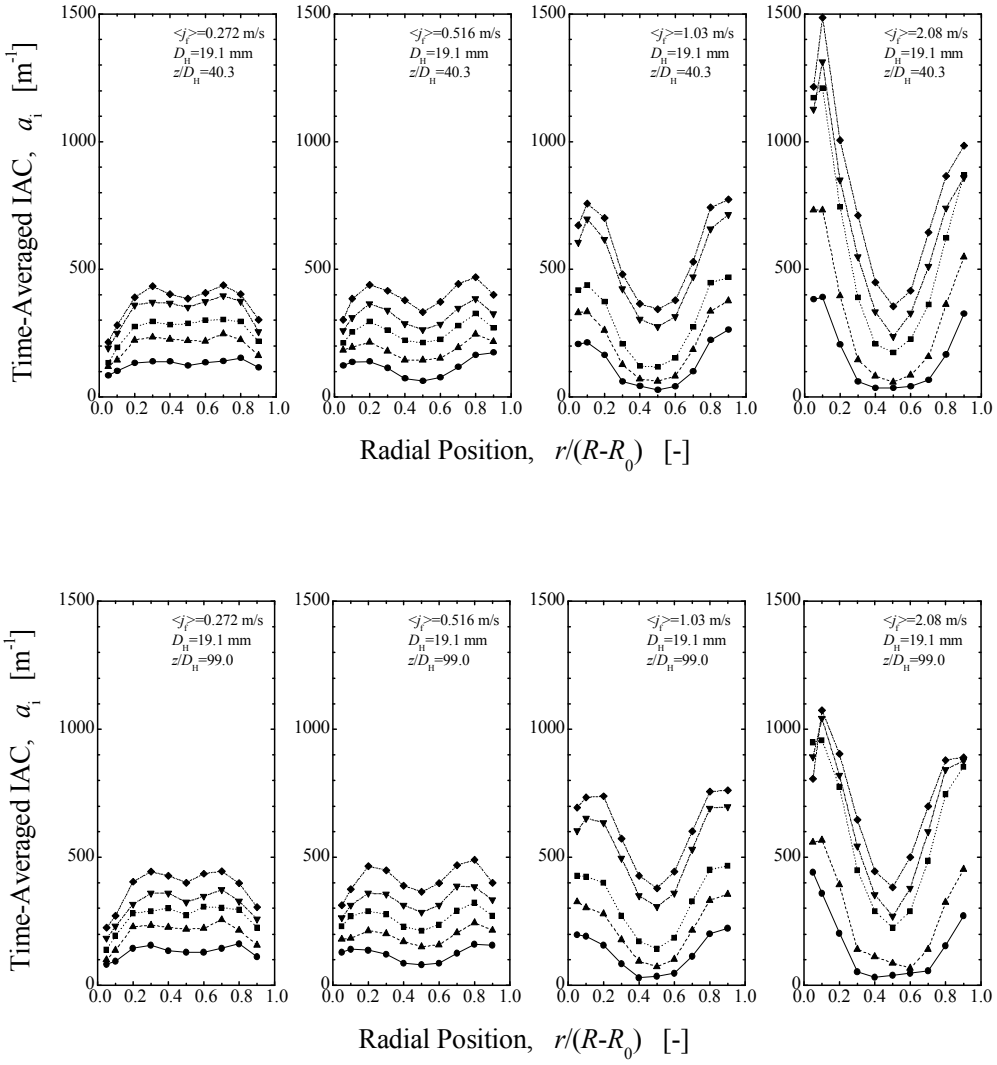
<j_f>=0.272 m/s
D_H=19.1 mm
z/D_H=40.3
<j_f>=0.516 m/s
D_H=19.1 mm
z/D_H=40.3
<j_f>=1.03 m/s
D_H=19.1 mm
z/D_H=40.3
<j_f>=2.08 m/s
D_H=19.1 mm
z/D_H=40.3
Time-Averaged IAC, a_i [m^{-1}]
Radial Position, $r/(R-R_0)$ [-]
<j_f>=0.272 m/s
D_H=19.1 mm
z/D_H=99.0
<j_f>=0.516 m/s
D_H=19.1 mm
z/D_H=99.0
<j_f>=1.03 m/s
D_H=19.1 mm
z/D_H=99.0
<j_f>=2.08 m/s
D_H=19.1 mm
z/D_H=99.0
Time-Averaged IAC, a_i [m^{-1}]
Radial Position, $r/(R-R_0)$ [-]

Fig.6

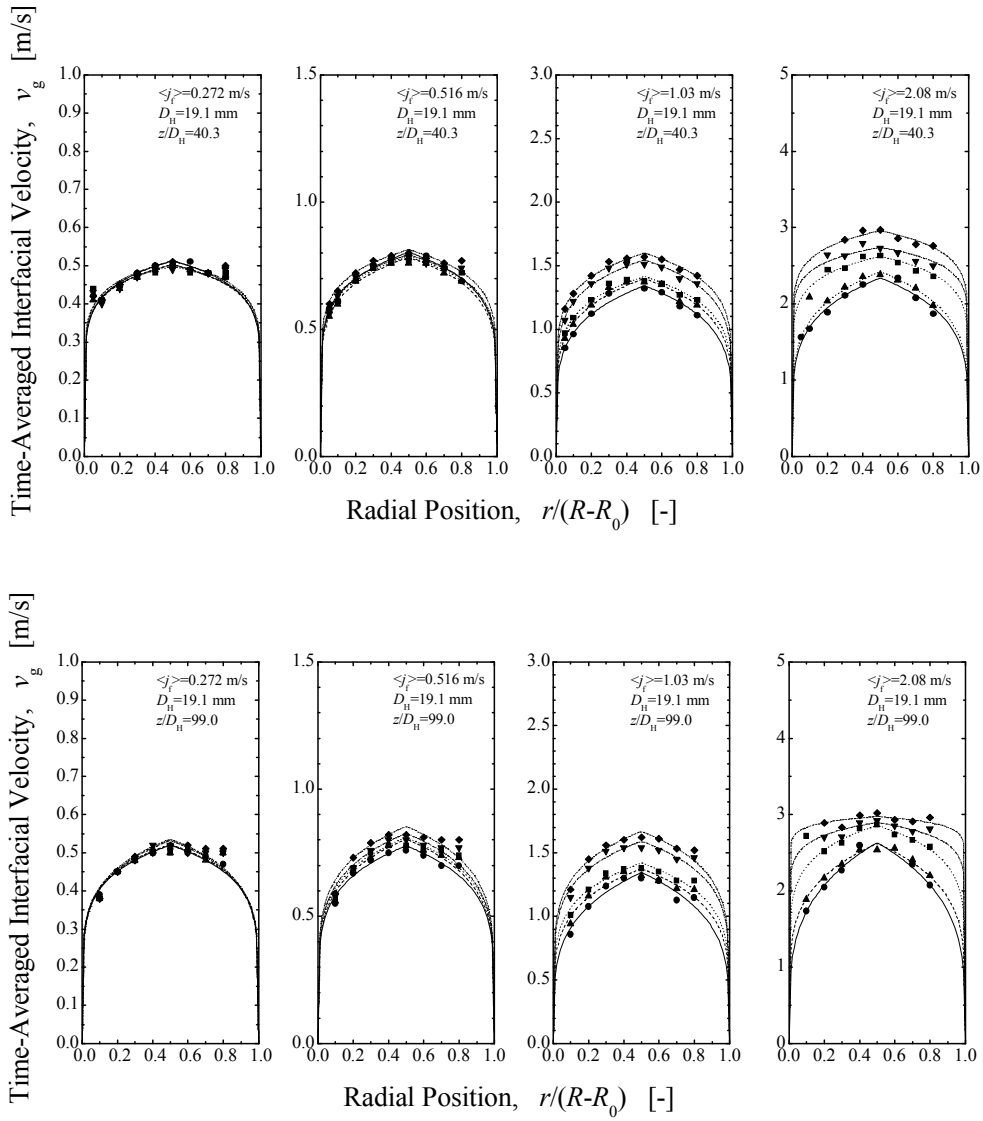
Time-Averaged Interfacial Velocity, v_g [m/s]
<j_f>=0.272 m/s
D_H=19.1 mm
z/D_H=40.3
<j_f>=0.516 m/s
D_H=19.1 mm
z/D_H=40.3
<j_f>=1.03 m/s
D_H=19.1 mm
z/D_H=40.3
<j_f>=2.08 m/s
D_H=19.1 mm
z/D_H=40.3
Radial Position, $r/(R-R_0)$ [-]
Time-Averaged Interfacial Velocity, v_g [m/s]
<j_f>=0.272 m/s
D_H=19.1 mm
z/D_H=99.0
<j_f>=0.516 m/s
D_H=19.1 mm
z/D_H=99.0
<j_f>=1.03 m/s
D_H=19.1 mm
z/D_H=99.0
<j_f>=2.08 m/s
D_H=19.1 mm
z/D_H=99.0
Radial Position, $r/(R-R_0)$ [-]

Fig.7

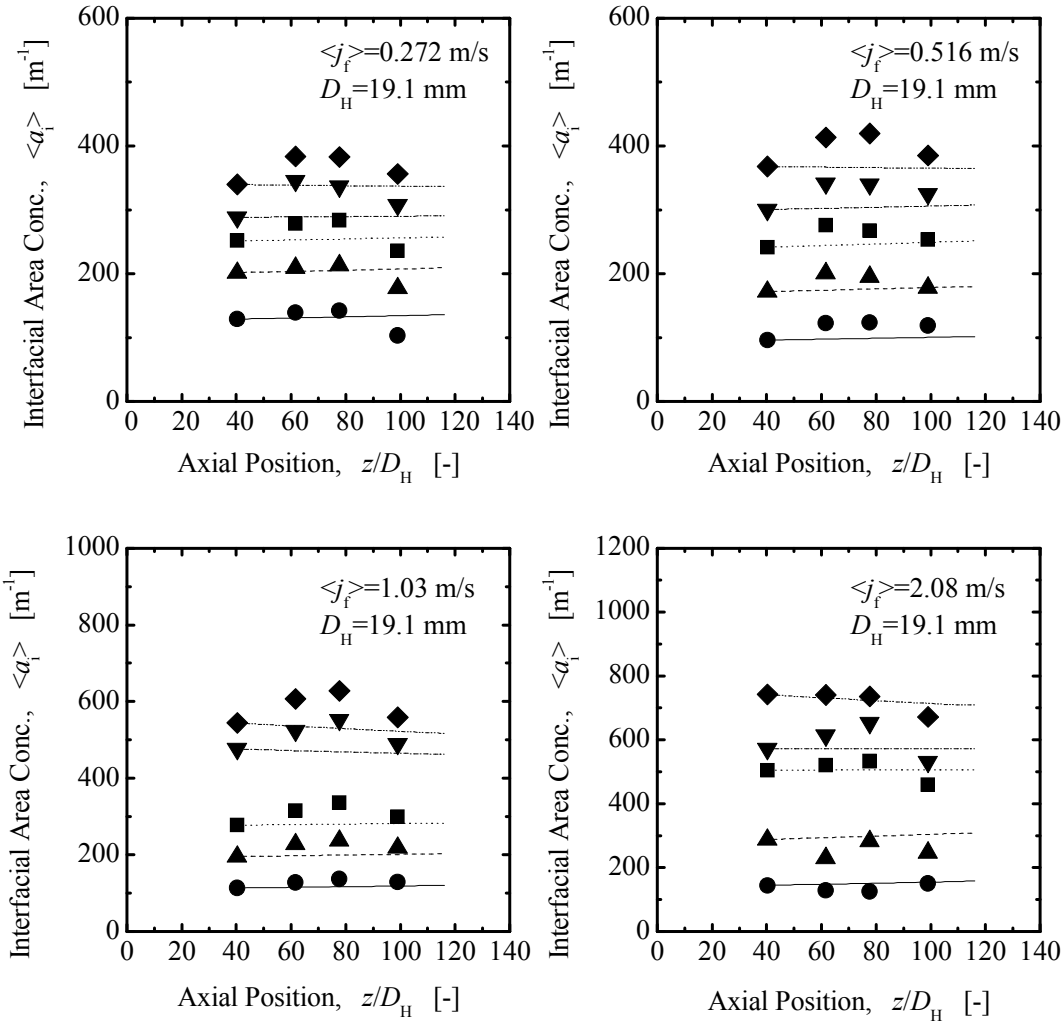
<j_f>=0.272 m/s
D_H=19.1 mm
<j_f>=0.516 m/s
D_H=19.1 mm
<j_f>=1.03 m/s
D_H=19.1 mm
<j_f>=2.08 m/s
D_H=19.1 mm
Interfacial Area Conc., <a_i> [m^{-1}]
Axial Position, z/D_H [-]

Fig.8

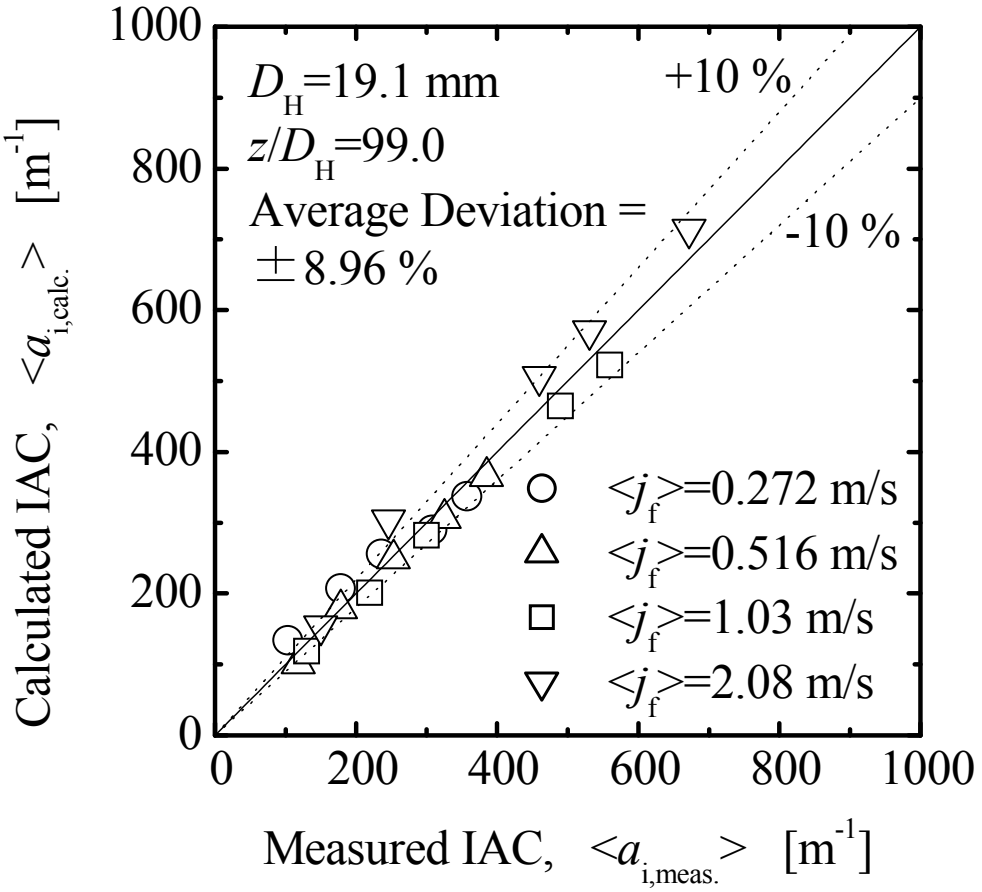
D_H=19.1 mm
z/D_H=99.0
Average Deviation =
±8.96 %
+10 %
-10 %
<j_f>=0.272 m/s
<j_f>=0.516 m/s
<j_f>=1.03 m/s
<j_f>=2.08 m/s
Calculated IAC, <$a_{i,calc.}$> [m^{-1}]
Measured IAC, <$a_{i,meas.}$> [m^{-1}]
0
200
400
600
800
1000

Fig.9

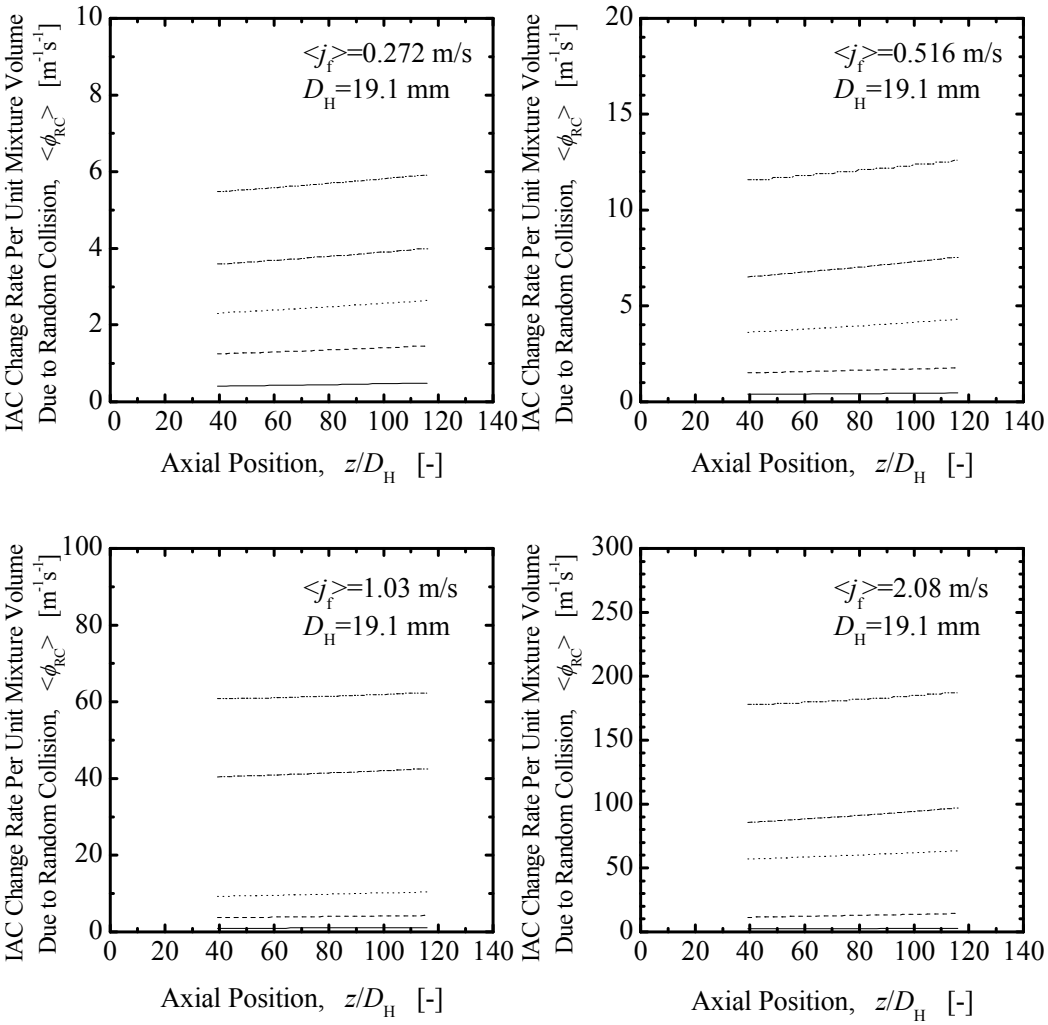
IAC Change Rate Per Unit Mixture Volume Due to Random Collision, <φRC> [m-1s-1]
<jf>=0.272 m/s
DH=19.1 mm
<jf>=0.516 m/s
DH=19.1 mm
<jf>=1.03 m/s
DH=19.1 mm
<jf>=2.08 m/s
DH=19.1 mm
Axial Position, z/DH [-]

Fig.10

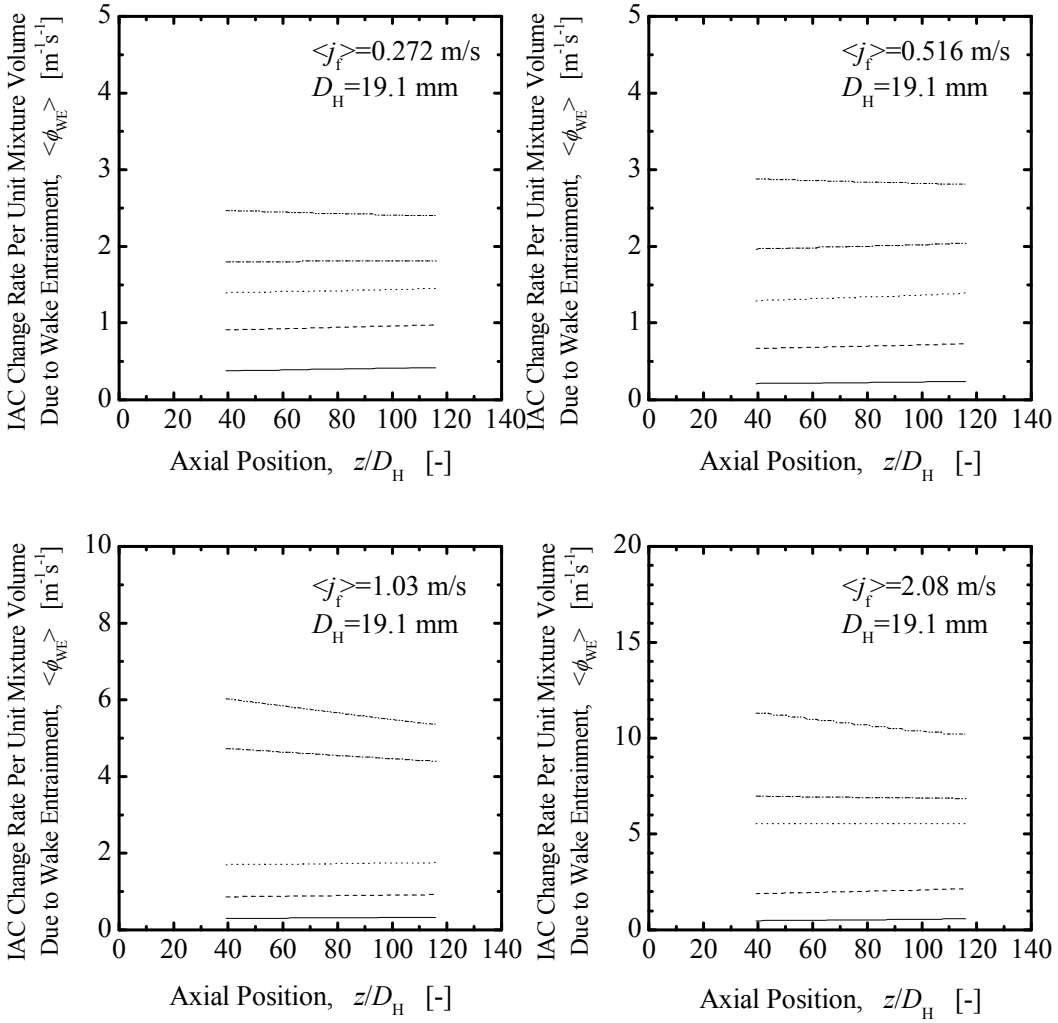
IAC Change Rate Per Unit Mixture Volume Due to Wake Entrainment, <φWE> [m-1s-1]
<jf>=0.272 m/s
DH=19.1 mm
<jf>=0.516 m/s
DH=19.1 mm
<jf>=1.03 m/s
DH=19.1 mm
<jf>=2.08 m/s
DH=19.1 mm
Axial Position, z/DH [-]

Fig.11

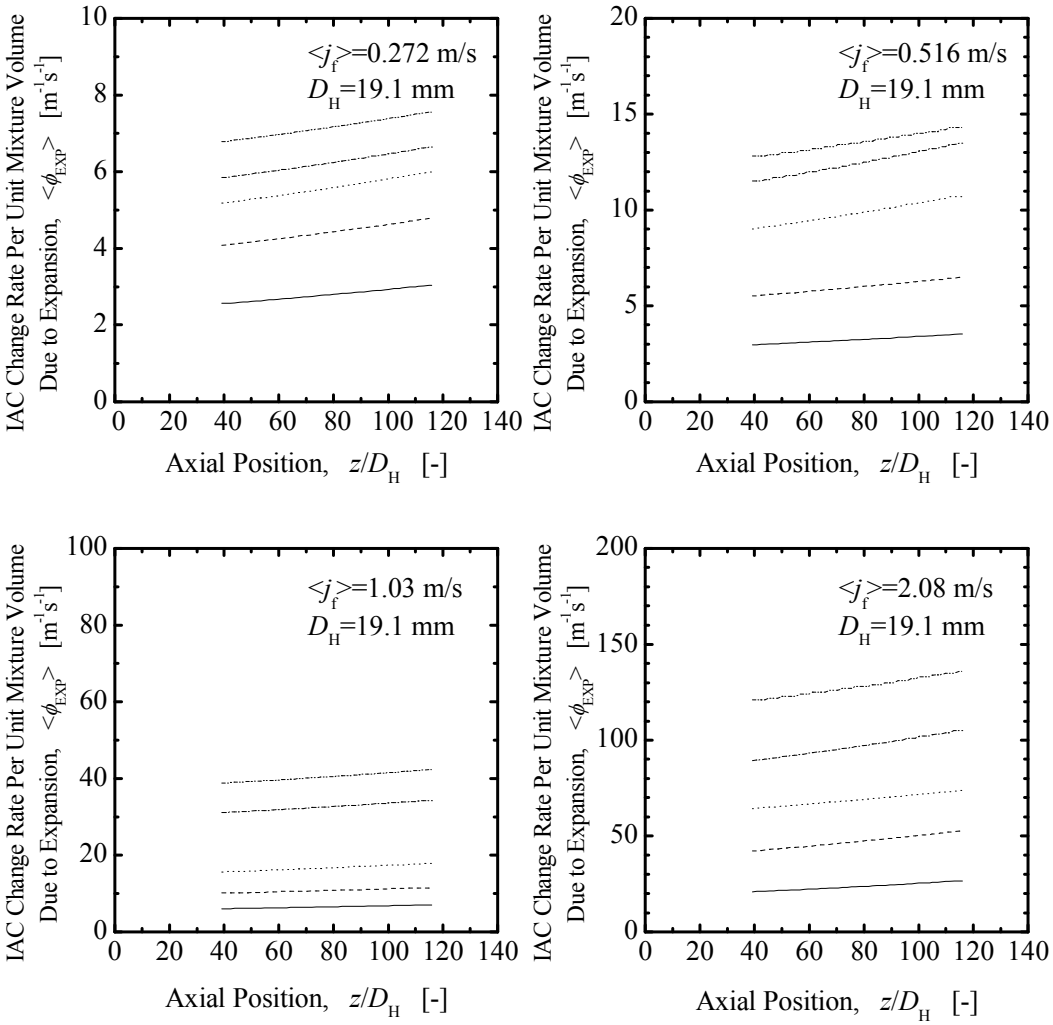
IAC Change Rate Per Unit Mixture Volume Due to Expansion, <φEXP> [m-1s-1]
Axial Position, z/DH [-]
<jf>=0.272 m/s
DH=19.1 mm
<jf>=0.516 m/s
DH=19.1 mm
<jf>=1.03 m/s
DH=19.1 mm
<jf>=2.08 m/s
DH=19.1 mm

Fig.12

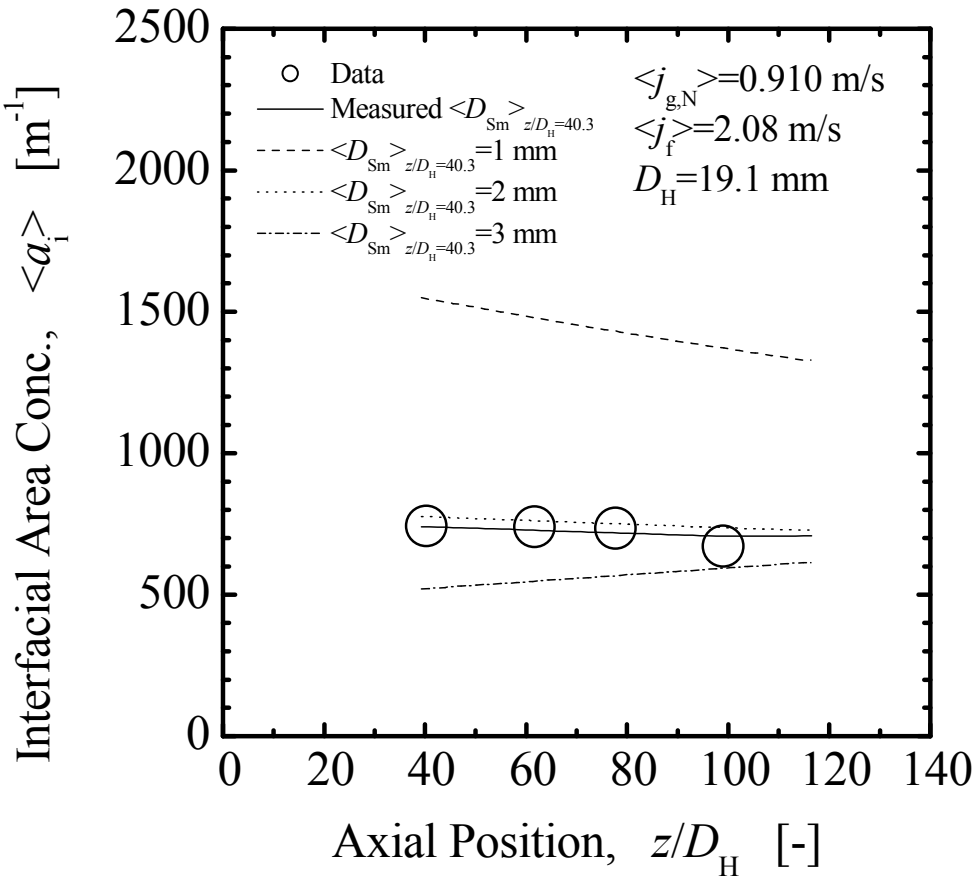
Data
Measured <D_{Sm}>$_{z/D_H=40.3}$
<D_{Sm}>$_{z/D_H=40.3}$=1 mm
<D_{Sm}>$_{z/D_H=40.3}$=2 mm
<D_{Sm}>$_{z/D_H=40.3}$=3 mm
<$j_{g,N}$>=0.910 m/s
<j_f>=2.08 m/s
D_H=19.1 mm
Interfacial Area Conc., <a_i> [m^{-1}]
Axial Position, z/D_H [-]
0
500
1000
1500
2000
2500
0
20
40
60
80
100
120
140

Fig.13